Cerebral Cortex Advance Access published February 8, 2013

Cerebral Cortex
doi:10.1093/cercor/bht022

Spatial Modules of Coherent Activity in Pathway-Specific LFPs in the Hippocampus Reflect Topology and Different Modes of Presynaptic Synchronization

N. Benito[1], A. Fernández-Ruiz[1], V.A. Makarov[2], J. Makarova[1], A. Korovaichuk[1] and O. Herreras[1]

[1]Department of Systems Neuroscience, Cajal Institute, CSIC, Madrid 28002, Spain and [2]Department of Applied Mathematics, Faculty of Mathematics, Universidad Complutense de Madrid, Madrid 28040, Spain

N.B. and A.F.-R. have contributed equally to this work.

Address correspondence to Oscar Herreras, Cajal Institute, CSIC, Av. Dr. Arce 37, Madrid 28002, Spain. Email: herreras@cajal.csic.es

Ongoing network activity often manifests as irregular fluctuations in local field potentials (LFPs), a complex mixture of multicellular synaptic currents of varying locations and extensions. Among other conditions, for synchronously firing presynaptic units to generate sizable postsynaptic LFPs, their axonal territories should overlap. We have taken advantage of anatomical regularity of the rat hippocampus and combined multiple linear recordings and spatial discrimination techniques to separate pathway-specific LFPs with enough spatial resolution to discriminate postsynaptic regions of varying activation, and to investigate their presynaptic origin, chemical nature, and spatial extension. We identified 6 main excitatory and inhibitory LFP generators with different synaptic territories in principal cells and hippocampal subfields matching anatomical pathways. Some recognized pathways did not contribute notably to LFPs. Each showed different septo-temporal spatial modules over which the field potential fluctuations were synchronous. These modules were explained by either the strong overlap of synaptic territories of coactivated afferent neurons (e.g., CA3 clusters for CA1 Schaffer LFPs), or widespread coalescence of postsynaptic territories (granule cell somatic inhibition). We also show evidence that distinct modes of afferent synchronization generate stereotyped spatial patterns of synchronous LFPs in one pathway. Thus, studying spatial coherence of pathway-specific LFPs provides remote access to the dynamics of afferent populations.

Keywords: correlated activity, independent component analysis, LFP generators, ongoing activity, spatial modules

Introduction

Correlated firing of neurons is often associated with shared synaptic inputs (Diesmann et al. 1999), which manifest as fluctuations of the local field potential (LFP; Bach and Kruger 1986; Arieli et al. 1995). This mesoscopic variable is mostly contributed by the postsynaptic currents (Purpura 1959; Elul 1972; Nunez and Srinivasan 2006), and as such LFP constitutes a link between the ongoing activity of afferent populations (distant and/or local) and the induced spatially distributed firing of postsynaptic neurons (Belitski et al. 2008; Fernández-Ruiz, Makarov, Benito, et al. 2012).

It has long been hypothesized that spontaneous macroscopic field potentials have a multifoci origin made up by the group of currents injected in the extracellular space by synchronously activated synapses, so called "elementary synaptic units" (Elul 1972). Such groups of coactivated synapses are located on multiple postsynaptic neurons according to axonal branching and topology, making up multineuron sources of complex geometry. Whereas the theoretical foundations describing how the spread of currents in a volume conductor raise field potentials of different magnitude and polarity are long established (Lorente de Nó 1947; Woodbury 1960; Plonsey 1969; Gloor 1985; Nunez and Srinivasan 2006), it was soon recognized that the geometrical complexity of these sources would be a handicap to decipher the cellular origins of LFP fluctuations. If axonal territories of synchronously firing presynaptic units overlap in the target postsynaptic region, the synaptic currents will have a chance to sum and raise sizable LFPs. However, due to variation in the spatial coverage of coactivated multineuron sources, the LFPs recorded at 2 nearby sites may be matched or different. The spatial extension, amplitude, and polarity of LFPs are influenced by a combination of factors including the patterns of synaptic territories of converging pathways, the topology of connections, and the time-dependent mixture of synaptic currents. We take the advantage of regular cytoarchitecture of the rat hippocampus, high-density recordings, and spatially discriminating analysis techniques (Bell and Sejnowski 1995; Choi et al. 2005) to address the pathway composition of ongoing LFPs and the time-varying spatial coverage of each component.

The hippocampus exhibits multiple naturally oscillating field potentials, including those displaying theta and gamma patterns (Buzsáki et al. 1983). These oscillations probably involve the synchronous activity of one or few synaptic pathways and have been widely used to study synaptic plasticity and the neuronal correlates of behavior (Paulsen and Moser 1998; Traub et al. 1998; Reichinnek et al. 2010). However, the physiological spectrum of ongoing LFPs contains a much wider collection of "irregular" activities that have been poorly studied and may provide valuable details as to the information arriving from multiple afferent populations to hippocampal principal neurons.

As it was demonstrated by the laminar analysis of evoked potentials (Andersen et al. 1971), the stratification of synaptic inputs into the discrete domains of postsynaptic cells produces distinct laminar field potential profiles upon activation of each afferent pathway (laminar dipoles). The difference between evoked and ongoing activities is in spatial extension of the activated postsynaptic region, occupying entirely, or in part, the synaptic territory of such input. We here asked whether the large irregular LFPs in the hippocampus arise as occasional spatiotemporal concurrence of synaptic currents from multiple independent presynaptic origins or they contain topographically determined modules of activity. If these modules exist, they should be related to anatomical pathways. Thus, we explored the existence of such spatial modules for different pathway-specific inputs (here termed as LFP generators) during ongoing activity by analyzing multiple

simultaneous recordings of the target populations in 3 steps. First, we determine all principal synaptic pathways that contribute to ongoing LFPs by separating their mixed contributions using multiarray linear recordings and analytical techniques, including independent component analysis (ICA; Makarov et al. 2010; Makarova et al. 2011). Secondly, we study their chemical nature and the neuronal populations of origin using local pharmacology and chemical manipulation of presynaptic nuclei. Finally, we explore their spatial coherence by comparing the time activations of each LFP generator in multiple sites along the septo-temporal axis and checked their stability upon different levels of presynaptic synchronization.

The results provide empirical evidence of the varying spatial extension of postsynaptic LFP generators brought about by the variable synchronization of presynaptic units. We found 6 main excitatory and inhibitory LFP generators in different subfields of the hippocampus, each corresponding to the postsynaptic activity elicited in distinct synaptic territories of principal pyramidal or granule cells by specific local and extrinsic afferent pathways. The septo-temporal extension over which each LFP generator was synchronous varied continuously during ongoing irregular LFP activity, reflecting the varying activation of presynaptic units with topographic projections. In some pathways such as the CA3 Schaffer input to CA1, we recognized different spatial patterns of synchronous postsynaptic activity that corresponded to stereotyped modes of presynaptic firing. Thus, the availability of spatial modules of pathway-specific activity allows the recognizable modes of functional organization to be identified in different segments of hippocampal networks.

Materials and Methods

Experimental Procedures

All experiments were performed in accordance with European Union guidelines (86/609/EU) and Spanish regulations (BOE 67/8509-12, 1988) regarding the use of laboratory animals, and the experimental protocols were approved by the Research Committee of the Cajal Institute. Adult female Sprague-Dawley rats were anesthetized with urethane (1.2 g/kg, intraperitoneally) and placed in a stereotaxic device. Surgical and stereotaxic procedures were performed as described previously (Herreras et al. 1988; Canals et al. 2005). Concentric stimulating electrodes were placed in one or more of the following sites in order to activate specific pathways and subfields: Ipsilateral CA3 region, and medial and lateral perforant pathways. Multisite silicon probes (Neuronexus, Ann Arbor, MI, USA) of 16 or 32 linear recording sites organized in 1 or 2 shanks were used to record in multiple tracks at steps of 50 or 100 μm parallel to the main axis of the CA1 pyramidal cell region, also spanning the dentate gyrus (DG)/CA3 regions. In experiments using multiple shanks, these were located along the long axis of the dorsal portion of the hippocampus, roughly parallel to the midline (AP, 4.5–6.5 and L, 2.6–3.5 mm). In a subset of experiments, additional glass pipettes were used to simultaneously record from multiple points at more lateral and ventral levels guided by evoked potentials. Linear probes were soaked in 1,1′-dioctadecyl-3,3,3',3'-tetramethylindocarbocyanine perchlorate (DiI) before insertion (Molecular Probes, Invitrogen, Carlsbad, CA, USA) to assess their placement in histological sections postmortem. A silver chloride wire implanted in the skin of the neck served as a reference for recordings. Signals were amplified and acquired using MultiChannel System (Reutlingen, Germany), and Axon (Molecular Devices, Sunnyvale, CA, USA) hardware and software were used for multisite and glass pipette recordings (50 and 20 kHz sampling rate, respectively).

The excitatory/inhibitory chemical nature of LFP generators was studied by the local application of neurotransmitter blockers via glass recording pipettes (7–10 μm at the tip). These were introduced at a 10° angle from the vertical and targeted loci within 300–500 μm of a linear probe at different strata of the CA1/DG subfields. Microdrops (50–100 pL) were pressure injected by a Picospritzer (General Valve, Fairfield, NJ, USA) and adjusted to limit drug effects to within 500 μm, as determined by the selective modulation of evoked potentials in the desired group of recording sites (Canals et al. 2005). Bicuculline methiodide (BIC; Sigma, St. Louis, MO, USA) or 6,7-dinitro-quinoline-2,3-dione (DNQX; Tocris, Bristol, UK) were loaded into the pipettes to block gamma amino butyric acid-A (GABA-A) and non-n-Methyl-D-Aspartate (NMDA) Glu receptors, respectively. Drugs were dissolved in artificial cerebrospinal fluid at concentrations of approximately 50 times higher than those usually employed in vitro. A single injection ensured stable effects of the drug for at least 60 s. In some experiments requiring longer drug actions, successive microdrops were injected at 5-min intervals, resulting in reasonable long-term stability witnessed by the steady effect on evoked potentials. In one set of experiments, BIC was injected from larger pipettes (10–12 μm at the tip) to achieve spatially extended hypersynchronous activity in neuronal populations projecting to recording loci (i.e., the afferent populations originating LFP components).

In a subset of experiments, recordings were obtained from awake animals implanted with a multishank device (92 recording sites in 6 parallel linear arrays). These data were obtained in the lab of G. Buzsáki using procedures for animal handling, surgery, and recording described previously (Montgomery et al. 2009).

At the end of each experiment, the animals were perfused through the abdominal aorta with phosphate buffer saline containing heparin (0.1%) followed by paraformaldehyde (4%), and the brains were processed for microscopic inspection. Sagittal sections (80 μm) were stained with bis-benzimide and examined by fluorescence microscopy for the assessment of the electrode positioning (Supplementary Fig. 1).

Independent Component and Current Source-Density Analyses of LFPs

ICA is routinely used to elucidate functional connectivity either in multisite scalp recordings or in functional magnetic resonance imaging, and it provides spatially stable components of coherent activity (Makeig et al. 1997; Van de Ven et al. 2004; Congedo et al. 2010; Hutchison et al. 2010). While the attribution of these ICA components to their source populations and pathways is difficult when recording from a distance, the in-source recording of intrahippocampal LFPs allows the thorough spatial inspection of active neurons down to the subcellular definition, and direct matching with the evoked potential profiles (Korovaichuk et al. 2010).

Detailed procedures have been previously described (Makarov et al. 2010; Fernández-Ruiz, Makarov, Benito, et al. 2012), and both the mathematical validation and the interpretation of ICA components in laminated structures were performed using realistic LFP modeling (Makarova et al. 2011). Briefly, M simultaneously recorded LFP signals were represented as the weighted sum of the activities of N neuronal sources or LFP generators:

$$u_m(t) = \sum_{n=1}^{N} V_{mn} s_n(t),$$

where $\{V_{mn}\}$ is the mixing matrix composed of the so-called voltage loadings or spatial distributions of all LFP generators and $s_n(t)$, the time course of the nth LFP generator. Thus, the raw LFP observed at the kth electrode tip is a linear mixture of the electrical activity of several independent LFP generators describing transmembrane current source densities (CSDs) in principal cells. Then, the CSD loading for the nth LFP generator is given by $I_n = -\sigma \Delta V_n$, where σ is the conductivity of the extracellular space (Makarov et al. 2010). As the location of recording sites is known, the joint curve of spatial weights of an LFP generator equals to instant depth profiles of proportional voltage among sites, as during the laminar recording of standard pathway-specific evoked potentials. To perform the ICA, we employed the kernel density ICA algorithm (Chen 2006), which returns the activations $s_n(t)$ and spatial weights V_n of up to N LFP

generators. Usually, few generators (4–7) exhibited significant amplitudes and distinct spatial distributions in the hippocampus (Korovaichuk et al. 2010). The spatial stability of LFP generators within and across animals was estimated using the cluster analysis of spatial curves as in Makarov et al. (2010) (Supplementary Fig. 2), whereas their landmarks (e.g., maxima or zero crossings) were matched to anatomical boundaries using electrophysiological correlates (unit firing at cell body layers and evoked potentials) and histological verification. The mixing matrix can be made with any number of simultaneous recordings, whether belonging to a single or multiple parallel arrays. Although, in the latter case, $s_n(t)$ represents spatially averaged activity, the combined spatial curve of weights is fully reliable and was used to evaluate the relative power of a given LFP generator in different hippocampal sites. The temporal accuracy of LFP generators can be cross-checked by analyzing the same LFP epochs using different number of contiguous electrodes (Supplementary Fig. 3). This procedure also served to increase the relative variance of an LFP generator by discarding the recordings where other generators introduced heavy variance, hence increasing the temporal accuracy by minimizing cross-contamination (Makarova et al. 2011). Once extracted from the raw LFPs, each LFP generator can be analyzed independently by reconstructing virtual LFPs produced by a single generator, $u_j(t) = V_j s_j(t)$ and then evaluating the current density created by this generator, the spatial profile of which allows comparison with profiles obtained during specific activation of known pathways (Makarova et al. 2011).

Current source-density analysis (Freeman and Nicholson 1975; Rappelsberger et al. 1981) determines the magnitude and location of the net transmembrane current generated by neuronal elements within a small region of tissue. Accordingly, we used the 1-dimensional approach, which calculates the CSD from the voltage gradients along the cells axis (Herreras 1990):

$$\mathrm{CSD} = -\sigma\Delta u = -\sigma\frac{u_{k-1}(t) - 2u_k(t) + u_{k+1}(t)}{h^2},$$

where h is the distance between recording sites. Admittedly, the spatial extent of current sources may not be large enough to fulfill the criterion of homogeneous activation in the XZ plane parallel to anatomical strata or laminae during asynchronous synaptic bombardment, thus tangential currents may introduce error in the amplitude estimate of sinks and sources (Leung 1979). Conveniently, the spatial distortion introduced by unbalanced tangential currents is effectively canceled out by time averaging of myriads microscopic currents as if they all were synchronously activated (Makarova et al. 2011). Thus, the curve of spatial weights for each LFP generator is accurate to the subcellular level. Although there is also a notable heterogeneity of tissue resistivity at the level of the st. pyramidale (López-Aguado et al. 2001), it introduces a negligible spatial distortion of depth profiles when active currents are located in distant dendritic loci. Thus, we have assumed homogeneous resistivity and used arbitrary units instead of CSD. In addition, we note that instant estimation of CSD along the entire anatomy of a cell generator (e.g., the CA1 pyramidal cell) does not render the balanced amount of inward and outward currents, while the CSD of reconstructed virtual LFPs for separated generators does (cf. in Fig. 1 of Fernández-Ruiz, Makarov, Benito, et al. 2012). This is a valuable side effect of the ICA when applied to laminar profiles covering the entire anatomy of cell generators: The separated components necessarily contain spatially coherent activity at any instant. Thus, for "in-source" recordings, the ICA acts as a rejection device for volume-conducted currents (Makarov et al. 2010; these may, however, come up in other ICA components). Consequently, the second spatial derivative of the curve of spatial weights of LFP components extracted for ongoing activity matches to that of the CSD, which was verified for excitatory pathways using the corresponding evoked potentials (Korovaichuk et al. 2010).

Quantifications of LFP Generators

The evolution of the power of an LFP generator over time is described (in mV^2) by the following equation: $P(t) = \int H(t-\tau)v^2(\tau)d\tau$, where $v(t)$ is the virtual LFP at the electrode with maximal power and H, the appropriately scaled square kernel of the length Δ. The mean power is then defined for Δ extended to the complete time interval (~10 min in our experiments).

The spatial extent of LFP generators was determined by estimating the cross-correlation index of the time envelopes or activations (10 min epochs) obtained for each LFP generator in different recording shanks (simultaneous recordings). We applied an ICA separately over each shank and then evaluated the pairwise cross-correlation index over time activations of the same LFP generator in different shanks.

The macroscopic spatial boundaries of each LFP generator across the hippocampal subfields were visualized by contour plots that built from the spatial curves of LFP generators separated through a joint analysis of all 96 simultaneous recordings arranged in 6 parallel linear shanks, that is, using a single loading matrix with all recordings that rendered a unique set of LFP generators. In this case, the unique time activation obtained for each generator is averaged over large extensions and, thus, it may not reflect local activity, although this was irrelevant when determining the spatial distributions. Faulty recording sites can be eliminated without significant performance loss of the ICA.

In a subset of experiments, the dynamic changes in the spatial extent of the LFP generators were examined by comparing the fine temporal details (activity) of a single generator in up to 4 different locations. For simplicity, we chose the excitatory Schaffer input from CA3 to CA1 that we had previously analyzed in depth (Fernández-Ruiz, Makarov, Benito, et al. 2012; Fernández-Ruiz, Makarov, Herreras 2012). The baseline activity of this generator is composed of a series of discrete field events or micro-field excitatory postsynaptic potentials (μ-fEPSPs). These are rhythmic excitatory packages in the gamma frequency that can be retrieved and quantified. We used the Wavelet Transform of $v(t)$:

$$W(a,b) = \frac{1}{\sqrt{a}}\int v(t)\psi\left(\frac{t-b}{a}\right)dt,$$

where ψ is the Haar mother wavelet (well suited for the detection of short pulses in a signal), a the time scale, and b the localization in time. We then rectified the wavelet coefficients using the following equation:

$$C(a,b) = \frac{1}{\sqrt{a}}\max[-W(a,b), 0],$$

The 2-dimensional (2D) surface obtained (Supplementary Fig. 4) describes the local linear fit of the Schaffer-specific LFP by the pulse-like function (Haar) at scale a and localization b. Large absolute values of $C(a,b)$ at a given time instant and scale correspond to abrupt pulse-like transitions in $v(t)$. Thus, we can associate such points in the (b,a)-plane with singular LFP events. Consequently, the local maxima of $C(a,b)$ evaluated as maxima over a set of small enough domains $\{\omega_k\}$

$$(a_k, b_k) = \arg\max_{(a,b)\in\omega_k}[C(a,b)],$$

define the time instants of μ-fEPSPs (given by $t_k = b_k - a_k/2$), their duration (given by a_k), and amplitudes (given by $A_k = C(a_k, b_k)$).

We next cross-correlated the μ-fEPSPs separately obtained in 2 locations and defined matching quanta for a time-window of ±2 ms (Supplementary Fig. 5). The amplitudes of paired μ-fEPSPs in different shanks were further plotted and cross-correlated evaluating the index: $r = c_{12}/\sqrt{c_{11}c_{22}}$, where $\{C_{ij}\}$ is the covariance matrix.

Spectral coherence of the activity of an LFP generator in 2 different spatial positions was calculated by:

$$C_{xy}(f) = \frac{|P_{xy}(f)|^2}{P_{xx}(f)P_{yy}(f)},$$

where $\{P_{ij}(f)\}$ is the matrix of crosspower spectral density. To determine the level of significance, we used the surrogate data test (Schreiber and Schmitz, 2000). Randomizing phase relations and keeping

other first order characteristics intact, we obtained surrogate time series from the original signals. For each experiment, we generated 1000 surrogates, and we evaluated spectral coherence. The significance level (at $\alpha = 0.05$) was then calculated for each frequency value and coherence above this level was considered statistically significant.

Results

Subcellular and Regional Extension of Main Hippocampal LFP Generators

To answer the generic question of why LFPs recorded nearby match or differ we need to know which anatomical pathways make synaptic contact near recording points, when each one becomes active, and the geometry of the current sources. Conveniently, several anatomical pathways arrive in stratified domains of principal cells, and their activation produces spatially stable synaptic currents and potentials that are pathway specific (Andersen et al. 1971; Leung 1979; Herreras 1990; Golarai and Sutula 1996), producing laminar spatial distribution of ongoing LFPs. These can be isolated by spatially discriminating techniques. Figure 1 illustrates the problem under study and the methodological approach. LFPs were recorded simultaneously along 2 parallel tracks spanning the CA1 and DG of the dorsal hippocampus (16 recording sites each, 100 μm apart, 500 μm between shanks). Recording sites within a linear array parallel to the main axis of principal pyramidal or granule cells explore different domains of nearby neurons. Recordings sites in different arrays serve to explore the multicellular (longitudinal) coverage of inputs by comparing recordings at similar dendritic levels. LFPs recorded in nearby electrodes may be very similar or differ significantly (Fig. 1*A*). In the illustrated example, while LFPs in the middle of the st. radiatum are nearly identical within and among arrays, those near the hippocampal fissure (hf) differ both in the vertical direction (i.e. different dendritic domains of nearby neurons), and in the horizontal plane (i.e. produced at the same dendritic level of multiple neurons in distant sites). Thus, the mixture of synaptic currents may already be hinted more complex and spatially restricted in some regions and neuron domains than in the others.

By inspecting multiple contiguous sites, bouts of activity of variable duration in stable spatial bands can be appreciated by the naked eye (Fig. 1*B*, boxed fragments). The stability of the group of electrodes showing similar activity indicates stable dendritic sites of synaptic activation by homogeneous afferent populations in accordance with anatomical data (Lorente de Nó 1934; Hjorth-Simonsen 1973). However, these bouts are usually overlapping in time and also in space, making unfeasible to ascribe LFP fluctuations to postsynaptic currents generated in one or another dendritic band. The site-specific LFP activities can be disentangled by the ICA into spatially stable independent LFP components or generators (Makarov et al. 2010; Korovaichuk et al. 2010; Makarova et al. 2011; Fernández-Ruiz, Makarov, Benito, et al. 2012; Fernández-Ruiz, Makarov, Herreras 2012; see Materials and Methods). The effectiveness of spatial separation can be appreciated by comparing the time courses of the raw LFPs with the activity of the first 3 LFP generators (Fig. 1*B* vs. *C*). Note that LFP fluctuations in the same group of electrodes at different moments were captured in the same LFP generator. Importantly, different procedures can prioritize either the spatial or temporal accuracy for specific components (see

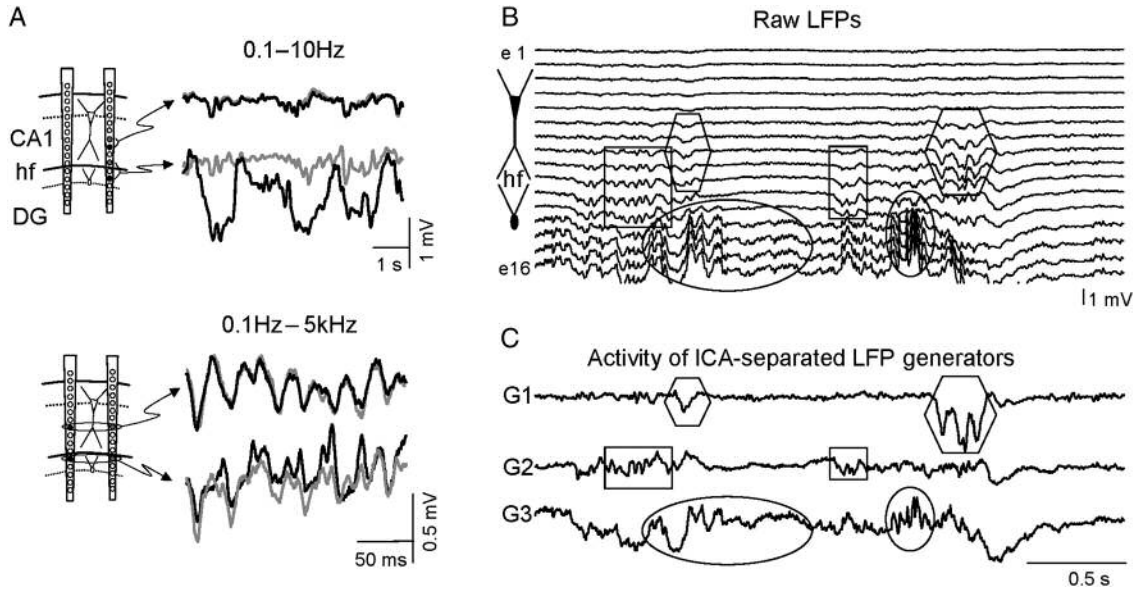

Figure 1. Hippocampal LFPs present laminar distribution and their multiple sources can be separated in domain-specific synaptic components. (*A*) Sketch of linear parallel 2 × 16 arrays spanning the CA1 and DG subfields, and examples of fragments of raw LFPs recorded in nearby positions (black or gray coding indicates the electrode positions and corresponding traces). LFPs can match or differ significantly at different positions and time points. The degree of similarity varies along the same vertical track (top panel) and within the same dendritic domain (bottom panel). For example, recordings from the CA1 stratum radiatum are strongly correlated in contiguous electrodes of the same array and between arrays, while significant differences are observed near the hf in both vertical and horizontal directions. Thus, the mixture of synaptic currents appears to be more complex and spatially restricted in some regions and neuronal domains than in others. (*B*) Representative recording of ongoing LFPs. Inset shows the location of the electrode array. Some bouts of activity spanning different groups of contiguous electrodes are shown in boxes to facilitate visual inspection. The spatial stability observed in the groups of electrodes with correlated activity indicates stable dendritic domains of the ongoing synaptic current sources. (*C*) Activity of 3 LFP generators separated by ICA from the LFP fragment shown in *B*. The effectiveness of the separated generators can be appreciated by visual comparison of the boxed bouts with their corresponding LFPs in *B*. If bouts in different generators overlap, then LFPs represent their weighted sum.

Materials and Methods), while the biophysical bases and limitations of the ICA when analyzing hippocampal LFPs have been thoroughly described elsewhere (Makarov et al. 2010; Makarova et al. 2011).

We first set out to define all primary stable dendritic domains of laminar LFPs. Except when indicated all results refer to anesthetized animals. We always chose epochs of irregular (nontheta) LFP activity for analysis as they contain a more balanced contribution of different synaptic inputs than macroscopic rhythms, in which one or few pathways may take most variance. We showed earlier that dominance of one input over others raises laminar LFPs that require additional signal handling as it reduces ICA performance on the weaker generators (Makarova et al. 2011).

We detected 6 main LFP generators that contained >99% of total variance in CA1/DG profiles and were stable in both anesthetized and awake animals (Figs 2 and 3). Gross classification was achieved by the cluster analysis of their curves of spatial weight obtained in 4–6 segments of 1 min in each animal (128–192 LFP components/animal; $n = 29$ animals in all experimental series; Methods and Supplementary Fig. 2). Only the generators that exhibited relative variance >1% in the complete CA1/DG (or CA1/CA3) profiles were examined, and the smaller generators that were detected but which exhibited very small or occasional activity were excluded from the analysis. Figure 2*A* shows raw LFPs along the axis of principal cells and the corresponding CSD profiles from a sample experiment. When generator-specific LFP (virtual) profiles were reconstructed (see Materials and Methods), each presented maximum activity in distinct dendritic domains of principal cells (4 sample generators are shown in Fig. 2*A*) and displayed only 1 maximum in a smooth spatial configuration. The LFP generators, G1 and G2, exhibited maximum power in the st. radiatum and lacunosum-moleculare (LM) of the CA1, respectively, although G2 also extended across the hippocampal fissure into the upper blade of the DG. Three more LFP generators (G3–G5) were located in the DG and their activity was strongest in the hilar region. Finally, an additional generator (G6) exhibited maximum variance in and around the CA3 pyramidal layer. Of all these generators the strongest were those located around the hippocampal fissure and dentate hilus (see population data for the relative variance and absolute power in Table 1).

The subcellular domains of each LFP generator can be approached by alignment of their respective spatial distributions to additional electrical landmarks, such as, for example, the population spikes in cell body layers. However, as LFPs extend beyond their current sources through volume conduction (Lorente de Nó 1947), we refined the subcellular location of active membranes by the CSD analysis of the depth profiles of LFPs that minimize the contribution of distant currents to recorded field potentials. This technique returns a spatial map of the transmembrane currents along the main axis of principal cells, which for the activation of a single pathway produces the laminated distribution of balanced inward (sinks) and outward currents (sources) circumscribed to the anatomy of the cell generator (Freeman and Nicholson 1975; Herreras 1990; see Materials and Methods). Due to the coactivation of multiple pathways, applying CSD to raw LFPs rendered an intricate mixture of currents (Fig. 2*A*). In contrast, the CSD obtained from the reconstructed generator-specific virtual LFPs (see Materials and Methods) rendered clean spatial maps with

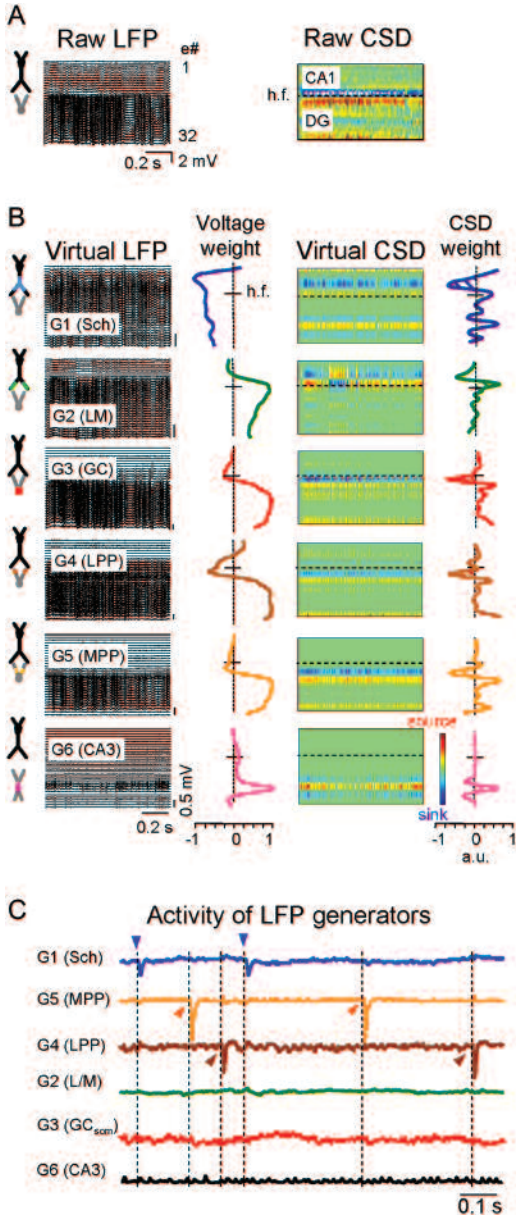

Figure 2. The subcellular localization of hippocampal LFP generators matches the termination zones of stratified synaptic pathways in discrete domains of principal cells. (*A*) Representative example of raw LFPs in a single electrode 1 × 32 array (left) and the corresponding CSD profile (right). The track spans from the CA1 soma layer to the inferior GC soma layer (pyramidal and granule cell dummies are represented to the left for spatial reference). Current sources are shown in red/yellow and sinks in blue. hf: hippocampal fissure. (*B*) Virtual LFP profiles and corresponding spatial weights reconstructed from ICA-separated LFP generators extend through discrete bands or strata with precise subcellular localizations. The CSD for each generator is restricted to a single cellular generator (CA1 or CA3 pyramidal cells, or granule cells). Except in one case (G2, in the CA1 st. lacunosum-moleculare; LM), all generators presented finite bands of inward or outward currents (no alternation in time) and smooth spatial profiles with only one maximum. Virtual CSD maps were obtained from virtual LFPs, and CSD weights (more noisy) are second spatial derivative of voltage weight curves. Hatched areas denote the dendritic bands where active (synaptic) currents were localized by local pharmacology (Fig. 4). CSD scale is in nonproportional arbitrary units to facilitate the visualization of weak currents. (*C*) Electric stimulation of major excitatory pathways produced evoked field EPSPs whose activity was selectively captured by the temporal activations of the respective LFP generators (scaled in proportional arbitrary units). Sch, medial perforant pathway (MPP), and lateral perforant pathway (LPP) stand for the Schaffer, medial and lateral perforant path generators, respectively. GC_{som}: granule cell soma generator. Colored triangles indicate stimulation times of the ipsilateral CA3, and the medial and lateral portions of the angular bundle. Note the negligible cross-contamination among generators. The vertical scale is shown in proportional arbitrary units.

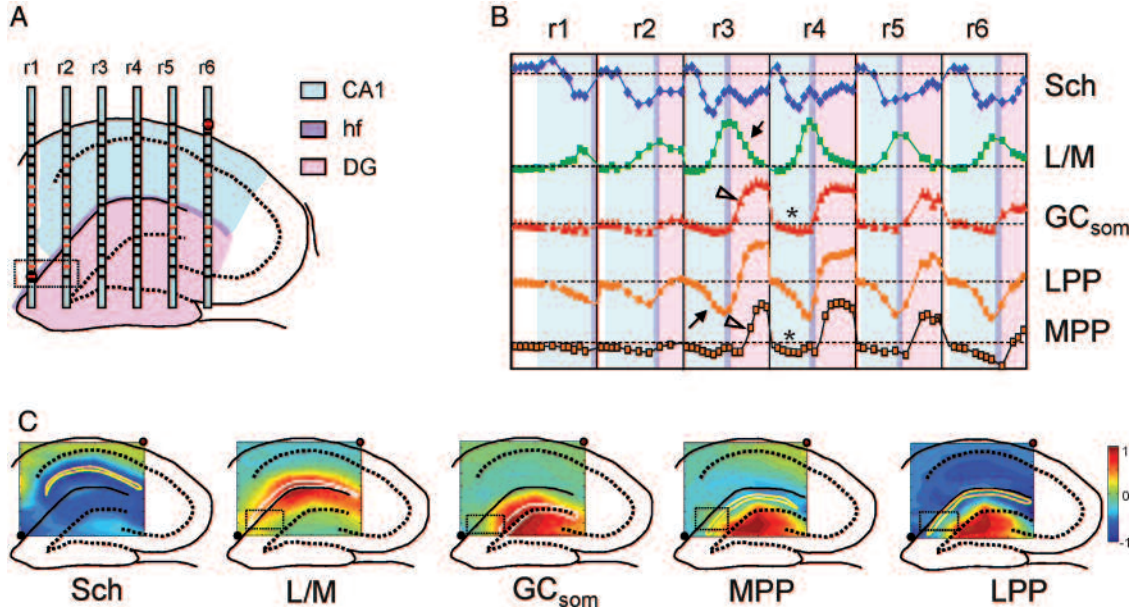

Figure 3. The regional distribution of LFP generators matches anatomical boundaries and hippocampal subfields. (*A*) Geometry of multiarray (r1–r6) chronic device showing the location of the recording shanks in hippocampal subfields (faulty electrodes are marked in red). (*B*) Representation of unfolded hippocampal subfields showing the spatial reconstruction of the relative weights corresponding to each isolated LFP generator. Note the repetitive spatial patterns and gradual shift of landmarks, such as the maxima or zero crossings, that remain at equivalent dendritic levels following the natural curvature of hippocampal layers. Black arrows indicate volume-conducted activity introduced in one subfield (CA1 or DG) by generators with active synaptic currents in distal dendritic domains of the other (LM, LPP). Generators with active currents in nondistal portions, such as the GC_{som} and MPP in the DG, generate little activity in remote areas (asterisks in CA1). Similar spatial profiles of some generators (GC_{som} and MPP) are efficiently discriminated by the abrupt shift in the spatial demarcation of the corresponding maxima (arrowhead) in the molecular layer of the DG. (*C*) Two-dimensional representation of virtual pathway-specific LFPs in hippocampal subfields indicating regional coverage, relative strength, and polarity (except for the LM generator in which polarity is unreliable). The active synaptic currents (identified by local pharmacology, see next figure) are defined by yellow or white lines, and the small squares indicate the zones of poor definition due to faulty electrodes.

Table 1
Relative variance and absolute power of ICA-separated LFP generators

LFP generator	Relative variance (%)	Mean power (mV^2)
Schaffer	10 ± 2	0.036 ± 0.01
Lac-Mol	23 ± 2	0.086 ± 0.02
MPP	7 ± 3	0.022 ± 0.01
LPP	32 ± 5	0.149 ± 0.04
GC_{som}	25 ± 5	0.116 ± 0.03
CA3	3 ± 1	0.017 ± 0.01

Note: The relative variance is measured as the percentage contribution among studied LFP generators found in profiles spanning the CA1 and DG. The mean power is estimated from reconstructed generator-specific LFP (virtual) profiles at the point of maximum weight in each generator. Values represent mean ± SEM.

characteristic smooth and simple laminar distributions of currents circumscribed to either the CA1 pyramidal cells (G1 and G2), granule cells (G3–G5), or CA3 pyramidal cells (G6). The hatched areas in the curves of spatial weights for the CSD indicate the active synaptic zones as determined by local pharmacology (Fig. 2*B*, see below). LFP generators in the DG were duplicated in both the upper and lower blades with a mirrored spatial distribution, and they exhibited no current in the hilus (except for errors created by spatial smoothing of discrete recording points). These spatial profiles were consistent with standard potential and CSD profiles of evoked synaptic activation in granule cells (McNaughton 1980; Golarai and Sutula 1996; Canning and Leung 1997; Korovaichuk et al. 2010). The so-called Schaffer generator (G1), with a characteristic spatial pattern of excitatory current sinks in the st. radiatum, was previously identified as the excitatory input from CA3 to CA1 (Korovaichuk et al. 2010; Fernández-Ruiz, Makarov, Benito, et al. 2012). The other CA1 LFP generator (G2 or LM generator), which extended across the hippocampal fissure, exhibited a temporal succession of current sinks and sources restricted to the st. LM. All 3 DG generators presented current sources in both granule cell layers and sinks in the corresponding molecular layers, albeit with distinct intensities and subcellular distribution. Thus, G3 (termed as GC_{som} generator) had strong sources in the granule cell layer, while G4 and G5 were characterized by strong narrow sinks in the medial and outer third of the molecular layer, respectively, and they were identified as the excitatory medial and lateral perforant path inputs to granule cells (medial perforant pathway [MPP] and lateral perforant pathway [LPP] generators; see distinct spatial curves in Fig. 3*A*) through the selective activation of the medial and lateral portions of the angular bundle, respectively (Fig. 2*C*). The LFP generator G6 was associated with strong current sources in the soma layer of CA3, and it was surrounded by sinks in both dendritic trees.

Next, we examined the regional extension of LFP generators. If LFP generators represent postsynaptic activity elicited by activity in distinct afferent populations, then each should exhibit regionalization in hippocampal subfields consistent with the spatial pattern of the axonal termination of that population. Therefore, we investigated the regional extension of the LFP generators in 2 awake animals in which multiarray electrodes were implanted (6 parallel shanks separated by 500 µm, Fig. 3*A*), and in 4 additional animals using single-array electrodes, plus numerous tracks in anesthetized animals. In awake animals, we analyzed recordings obtained

during nontheta behaviors (while still alert, as well as during consummatory tasks and slow-wave sleep), and spatially stable LFP generators across 6-shank arrays (Fig. 3*A*) were obtained by building a single matrix for analysis covering different dendritic levels and hippocampal subfields (77 of 96 useful channels in the experiment of Fig. 3). Analysis of the multiple segments of LFPs revealed identical sets of main generators to those found in multiple recording tracks in anesthetized animals. By representing the relative weights at each recording site we obtained combined spatial curves for all the arrays that revealed distinct spatial patterns fitting the anatomical boundaries of the hippocampal subfields. Each generator featured landmarks such as maxima and zero crossings that gradually shifted within the recording sites in parallel arrays matching the curved anatomy of the hippocampus such that they coincided at the same dendritic level (Fig. 3*B*, and see the 2D spatial configuration of the LFP generators illustrated in Fig. 3*C*). Note that LM and LPP generators whose active synaptic domains are located in the distal dendrites of CA1 pyramidal and granule cells, respectively, entered notable field potential into the adjacent subfield by volume conduction (Fig. 3*B*, black arrows), while this was not observed for MPP and GC_{som} generators (asterisks). It was also notable that there were dominant positive field potentials in the DG generators in the hilus generated through the volume conduction of currents from granule cell membranes. Despite the apparent similarity between MPP, LPP, and GC_{som} generators, these were readily discriminated by a persistent spatial shift in their respective distributions at the st. moleculare-granule cell border (e.g., arrowheads in r3, Fig. 3*B*; see additional evidence below).

Excitatory and Inhibitory LFP Generators

Using selective stimulation of principal extrinsic and associational pathways, we previously obtained data supporting the presynaptic origin of some excitatory LFP generators (Korovaichuk et al. 2010; see also Fig. 2*C*). Further evidence of the excitatory/inhibitory nature of all LFP generators was achieved by a local blockade of non-NMDA or GABA-A synaptic receptors using DNQX and BIC, respectively. As both excitatory and inhibitory synaptic inputs produce the loops of transmembrane currents with clearly discernible subcellular inward (sinks) and outward (sources) domains, we searched for the active bands (the site of synaptic contacts) by pharmacologically targeting each input. This was achieved by releasing a microdrop (50 nL) containing DNQX (1 mM) and DiI (4%) in the vicinity of the caudal shank of a 2-shank probe at the level of the CA1 st. radiatum (Fig. 4*A*). The Glu-R blocker selectively reduced the Schaffer-evoked fEPSP in the caudal shank, whereas no effects were observed on the rostral shank located 500 µm away, in concordance with the extension of the dye. The spatially localized effect of the drug can be also appreciated in the curves of the spatial weights that reflect a selective decrease of variance at the Schaffer terminal zone in the group of electrodes associated with the caudal shank. Moreover, DNQX only reduced Schaffer-evoked fEPSPs and ongoing Sch-LFPs when administered in the st. radiatum, but not in the soma layer or st. oriens (Supplementary Fig. 6). This procedure allows the synaptic areas and chemical nature of all 6 LFP generators to be identified.

Accordingly, the mean power for each virtual LFP was estimated over 200-s segments before and after drug administration in the following regions: The CA1 st. radiatum and lac.-mol for the Sch and LM generators, respectively; the st. moleculare of the DG for the MPP and LPP generators, the granule cell layer for the GC_{som} generator, and the CA3 pyramidal cell layer for the CA3 generator (see representative results and the population data for the effective sites in Fig. 4*B*,*C*, respectively). DNQX dramatically dampened the activity of the Sch, MPP, and LPP generators ($29.2 \pm 9.9\%$; $15.7 \pm 6.5\%$; $7.5 \pm 3.0\%$; $P < 0.01$, Student's *t*-test), whereas the LM, GC_{som}, and $CA3_{som}$ generators were affected by both BIC and DNQX, although a significant decrease in the GC_{som} generator was only observed in response to DNQX ($n = 4$, $^{**}P < 0.01$, Student's *t*-test: Fig. 4*C*). While the antagonistic effect of BIC indicates a GABAergic origin, the reduction in power observed in the same LFP generator following Glu-R blockade indicates either a combination of 2 synaptic LFP generators (1 excitatory and 1 inhibitory), or a reduction in the excitatory drive of a single inhibitory pathway from local interneurons with somatodendritic bodies and axonal projections in the same spatial domain. The narrow domains of the active synaptic (outwards) currents produced by LM and GC_{som} generators are suggestive of inputs from subpopulations of interneurons with axon terminals at distal apical dendrites of CA1 pyramidal cells and granule cell somata, respectively.

Minimum Spatial Modules of Correlation for Pathway-Specific LFPs

The spatial correlation of LFPs (Fig. 1*B*) indicates the similarity of the time envelopes of postsynaptic currents at distinct loci. We first sought evidence of anatomical determinants that might underlie the spatial correlation by searching for the minimum modules in which pathway-specific LFPs remain invariant. For this purpose, we recorded LFPs simultaneously using 2 double-shank probes that were relocated in successive sessions (Fig. 5*A*). We then estimated the mean correlation coefficient between the temporal envelopes of the same LFP generator (1 min epochs) measured separately at different locations in a rostro-caudal gradient. For this purpose, we analyzed 2 excitatory (Sch and MPP) and 2 inhibitory (LM and GC_{som}) LFP generators.

As expected, the spatial correlation of all LFP generators diminished over distance, although at marked generator-specific rates. Superimposed fragments following GC_{som} activation (Fig. 5*B*) show a close correlation, even for distant loci (points 1 vs. 6), which contrasted with the strong divergence evident for the MPP generator (points 3 vs. 4), even at short distances (see the population data in Fig. 5*C*, $n = 3$–10 animals). At a distance of 1 mm, a strong spatial correlation was observed for the inhibitory LFP generators in both the CA1 (LM) and DG (GC_{som}), with a mean correlation of 0.6 ± 0.01 ($n = 4$) and 0.8 ± 0.01 ($n = 4$), respectively. A very strong correlation was maintained for the excitatory Sch generator at distances of up to 1.5 mm (0.75 ± 0.1, $n = 5$: Excluding sharp-wave (SPW) events, the correlation never fell <0.9), and this decayed gradually as the distances augmented. In contrast, a strong correlation was only observed for the MPP generator at 200 µm (0.89 ± 0.1; $n = 4$), which fell abruptly at distances ≥500 µm (0.33 ± 0.1; $n = 7$).

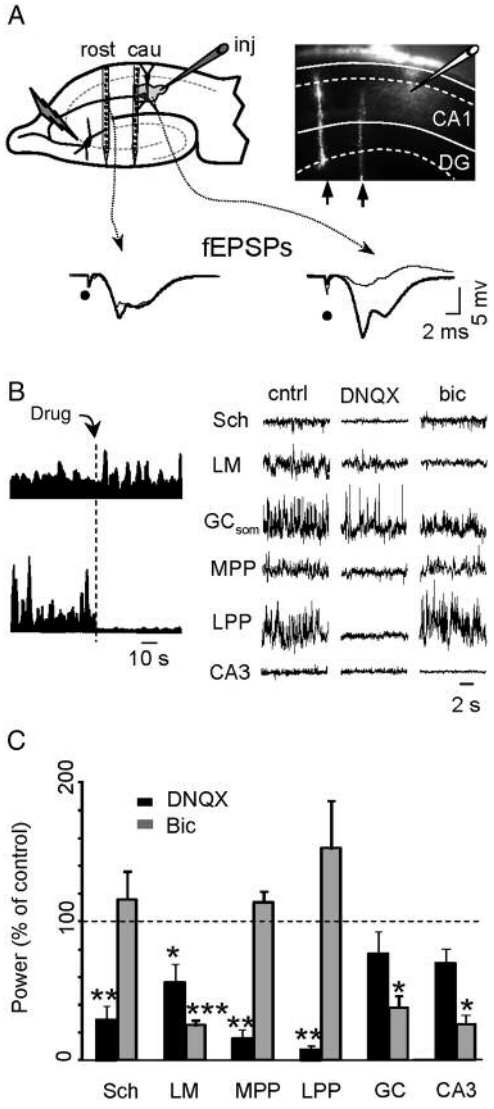

Figure 4. Chemical nature of hippocampal LFP generators. (*A*) Electrode arrangement and experimental procedure (left panel). Two-shank linear devices recorded in tracks 500 μm apart, and a recording/injecting pipette was used to inject different neurotransmitter blockers within 500 μm of one of the shanks at the desired dendritic level and subfield. The position of the recording arrays was verified by the DiI tracks revealed after histological processing, as well as the extent of injected volume in the st. radiatum of the CA1 field (right panel). The local effects of DiI were restricted to one of the arrays, with no effects observed at the second array. Note the selective reduction of Schaffer-evoked fEPSP in the caudal shank (bottom subplot). (*B*) Representative experiment showing the sustained and selective effect of BIC on 1 of the 2 LFP generators extracted from the same vertical profile (left). The plots correspond to time envelopes of the mean power at the site of maximal activity (sliding window of 0.5 s) for the Schaffer (upper) and LM (lower) generators. The effects of DNQX and BIC on the activation of different LFP generators are shown on the right. The vertical scale is shown in arbitrary units. (*C*) Population data showing the effect of neurotransmitter blockade on LFP generators. The data (mean ± standard error of the mean [SEM]) represent the percentage of power in the drug-affected array relative to the unaffected array. $N = 4$–10 animals, except for CA3 generator ($n = 2$); Student's *t*-test: $^{*}P < 0.05$, $^{**}P < 0.005$, $^{***}P < 0.001$.

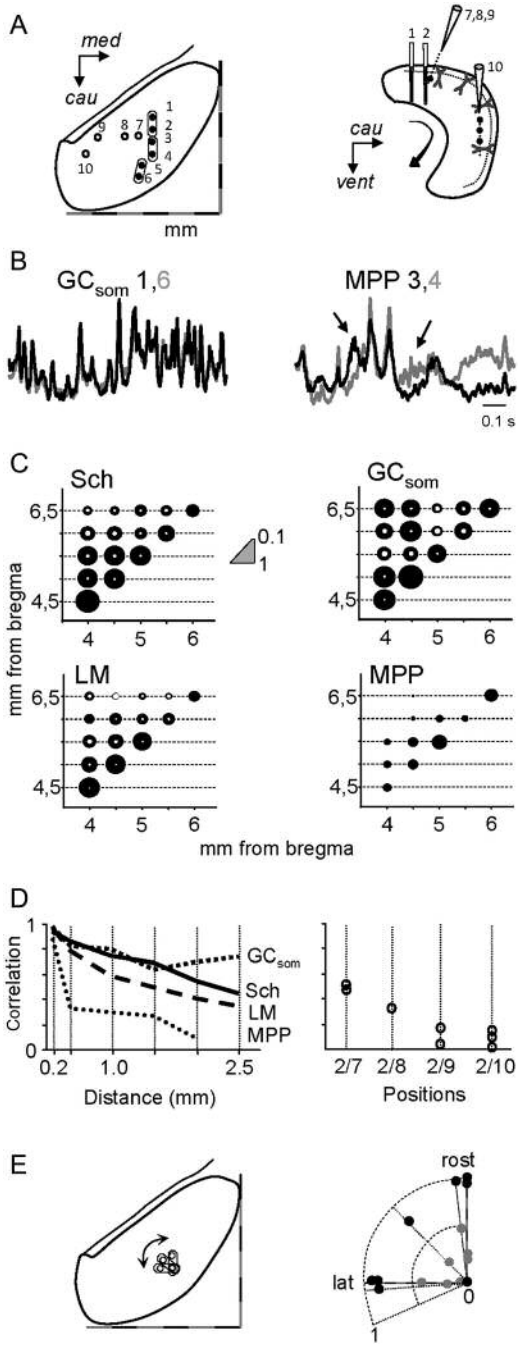

Figure 5. LFP generators show pathway-specific modules of spatial coherence. (*A*) Scheme showing the insertion points (left, dorsal view and right, lateral view) of parallel linear arrays (2 two-shank arrays inserted simultaneously) spanning the CA1 and DG (points 1–6), and the additional recording points in the CA1 st. radiatum (7–10). Two-shank arrays are enclosed in ovals. (*B*) Superimposed sample traces in 2 different arrays for the GC_{som} (left) and the MPP (right) generators. Note that distant positions (1 and 6) in the former exhibit nearly identical time courses, while nearby positions (3 and 4) in the latter differ significantly. (*C*) Cross-correlation coefficients for different LFP generators in positions roughly parallel to the midline (points 1–6; scale in absolute mm from bregma). Inner white circles represent the standard errors. (*D*) Left, comparative view of the degree of the spatial correlation for different LFP generators in loci parallels to the midline in a representative animal. Data are pooled according to the distances between the paired recording points (points 1–6). Right, additional comparisons for the Schaffer generator between the array at point 3 and single points in distinct ventro-lateral positions (data pooled from 3 animals). (*E*) Rotating the relative positions of the parallel arrays (500 μm separation) with respect to the midline does not noticeably modify the correlation. The data correspond to individual comparisons for the GC_{som} (black circles) and MPP (gray circles) generators pooled from 4 animals.

The decay rate of the spatial correlation for the 4 selected LFP generators was studied (Fig. 5*D*, left) and, although the hippocampal curvature complicates the correct placement of the arrays in central and ventral positions, we could obtain long-distance correlations for the Sch generator by using single-channel raw LFPs recorded by a micropipette in a

limited band in the st. radiatum in which we assessed that Sch-LFPs are poorly contaminated by distal LM sources (Supplementary Fig. 7). Thus, raw LFPs in these Schaffer-specific sites (Fig. 5*A*, right) were correlated with the time activation of the Sch generator in dorsal arrays (Fig. 5*D*, right). The correlation fell <0.2 for distances >2 mm and approached zero over longer distances, suggesting the existence of separate groups of activating presynaptic cells in the CA3 population.

In a separate set of experiments, we checked for the possible influence of diverse geometry and orientation of axonal terminal fields (Ishizuka et al. 1990; Somogyi and Klausberger 2005) by rotating 2-shank probes respect to the midline (Fig. 5*E*1). At least for the short distance tested (0.5 mm between shanks), we found identical high and low correlation for both the Sch (Fig. 5*E*, right, black circles) and MPP generators (gray circles), respectively ($n = 3$ animals).

Globally, these results indicate pathway-specific structural (anatomical) modules of invariant LFPs, which are largest for the granule cell somatic inhibitory input, very small for the excitatory MPP generator, and very large for the excitatory Schaffer generator only within strips parallel to the midline but decaying gradually along the longitudinal axis of the hippocampus.

The Match/Mismatch of Activity in LFP Generators Reveals Specific Topology and the Dynamics of Afferent Populations

A spatial module of correlated LFPs may be created by the synchronous firing of presynaptic units whose synaptic territories overlap heavily, or by joint modulation of the firing rate of presynaptic units whose projections do not necessarily overlap. We studied both these possibilities in the 2 LFP generators exhibiting large modules of strong spatial correlation, the excitatory Sch input to CA1, and the inhibitory GC_{som} input to DG, comparing the fine temporal structure of the fluctuations of each generator in site pairs (Fig. 6*A*1).

Time envelopes, estimated as instant variations in power, exhibited near identical patterns for the Schaffer generator at any 2 sites parallel to the midline (Fig. 6*A*2, points 1–2: Correlation 0.93 ± 0.02, positions 4–4.5 mm posterior to bregma, $n = 7$ measurements in 4 animals), and this correlation only dropped significantly when distant sites were compared in which one of the recordings was near the subicular border (points 1–6: 0.35 ± 0.07; $n = 4$). This decrease was induced largely by the dissimilar spatial coverage of SPWs occurring at low rates in periods of irregular nontheta activity (common and site-specific SPWs are indicated with filled and empty triangles and arrows, respectively: Fig. 6*A*2, see the sample cluster of SPWs in Fig. 6*A*3). Cross-correlation between Schaffer activations in dorso-medial (points 2–3) and latero-ventral positions (points 7–8) fell to negligible values, irrespective of the SPWs (0.13 ± 0.02, $n = 6$ comparisons in 2 animals: sample in Fig. 6*A*2, points 3 and 8), indicating that different groups of presynaptic CA3 cells project to laterally shifted (i.e., septo-temporal) CA1 sites.

Baseline Schaffer activity consisted of a gamma sequence of discrete field events in CA1 or μ-fEPSPs elicited by the sequential firing of CA3 neuronal assemblies (Fernández-Ruiz, Makarov, Benito, et al. 2012; Fernández-Ruiz, Makarov, Herreras 2012). These excitatory quanta exhibited a steady rostro-caudal delay of 2.0 ± 0.22 m/s ($n = 9$) that roughly approached the conduction velocity of Schaffer collaterals measured by evoked potentials (Andersen et al. 1971). In addition, there was a strong covariation in the amplitude of elementary μ-fEPSPs at sites parallel to the midline (Fig. 6*B*1), denoting a common set of presynaptic units (or functional assembly) that each generated a μ-fEPSP. The covariation index was estimated by linear regression between paired series of μ-fEPSPs independently obtained for each linear array and was 0.92 ± 0.3 between pairs of CA1 sites lying 4–6 mm posterior to the bregma (see sample in Fig. 6*A*1,*A*2, $n = 11$ measurements pooled from 4 animals), although it dropped to non-significant values as one of the recordings shifted laterally and ventrally ($r = 0.17 \pm 0.02$, $n = 6$ measurements pooled from 3 animals; Fig. 6*B*3). The percentage of paired μ-fEPSPs also dropped from $74.1 \pm 3.1\%$ to $46 \pm 0.8\%$ (~20–30% of non-paired events corresponded to noise-level events; see Materials and Methods). Finally, we evaluated the spectral coherence between pairs of recordings taken at different distances within the spatially correlated modules (see Materials and Methods). Analysis of 36 epochs (1 min each) in 4 animals rendered a smooth repeatable frequency profile in which the coherence was >0.8 for frequencies up to approximately 50 Hz and that decayed gradually to become nonsignificant beyond approximately 100 Hz (Fig. 6*C*, upper row).

When the GC_{som} was compared with the Sch generator, there were both similarities and notable differences within their respective modules of coherence. Both exhibited a dominant gamma succession of events (Figs 5*B* and 6*B*), although the GC_{som} exhibited no significant delay of paired elementary events recorded in different sites (0.09 ± 0.11 ms; $n = 16$ measurements pooled from 4 animals), indicating that spike conduction through the axonal arborization of presynaptic cells reached postsynaptic targets more synchronously. Furthermore, despite the strong global correlation between distant sites (up to 2.5 mm: Fig. 5*C*), the profiles of spectral coherence for the GC_{som} generator were more irregular between animals and varied in different epochs analyzed in the same animal (Fig. 6*C*, Experiment 3). Thus, while the spatial module of the coherence of the GC_{som} is compatible with a joint modulation of the firing rate of multiple presynaptic units projecting over the granule cell population (Whittington et al. 1995), the individual synaptic territories may not overlap significantly, permitting independent contributions to local LFPs according to processing demands.

Varying Synchronization of Presynaptic Units also Determines the Extent of Spatial Coherence

The aforementioned results indicate that anatomical constraints (e.g. overlapped postsynaptic territories of different Schaffer axons) may determine spatial coherence over large postsynaptic regions. However, naturally occurring variations in the synchronization of presynaptic units also determine the extent of spatial coherence. One such case is evident in the spatial coverage of basal and SPW activities in the Schaffer generator. Unlike elementary μ-fEPSPs, different SPW events covered variable portions of the dorsal CA1 (Fig. 6*A*3).

To further test this issue, we devised a functional test to externally modify the synchronization of firing in the afferent population/s. We checked 2 LFP generators with both high and low spatial coherence, the Schaffer and MPP excitatory generators, the activity of which is driven by the ipsilateral

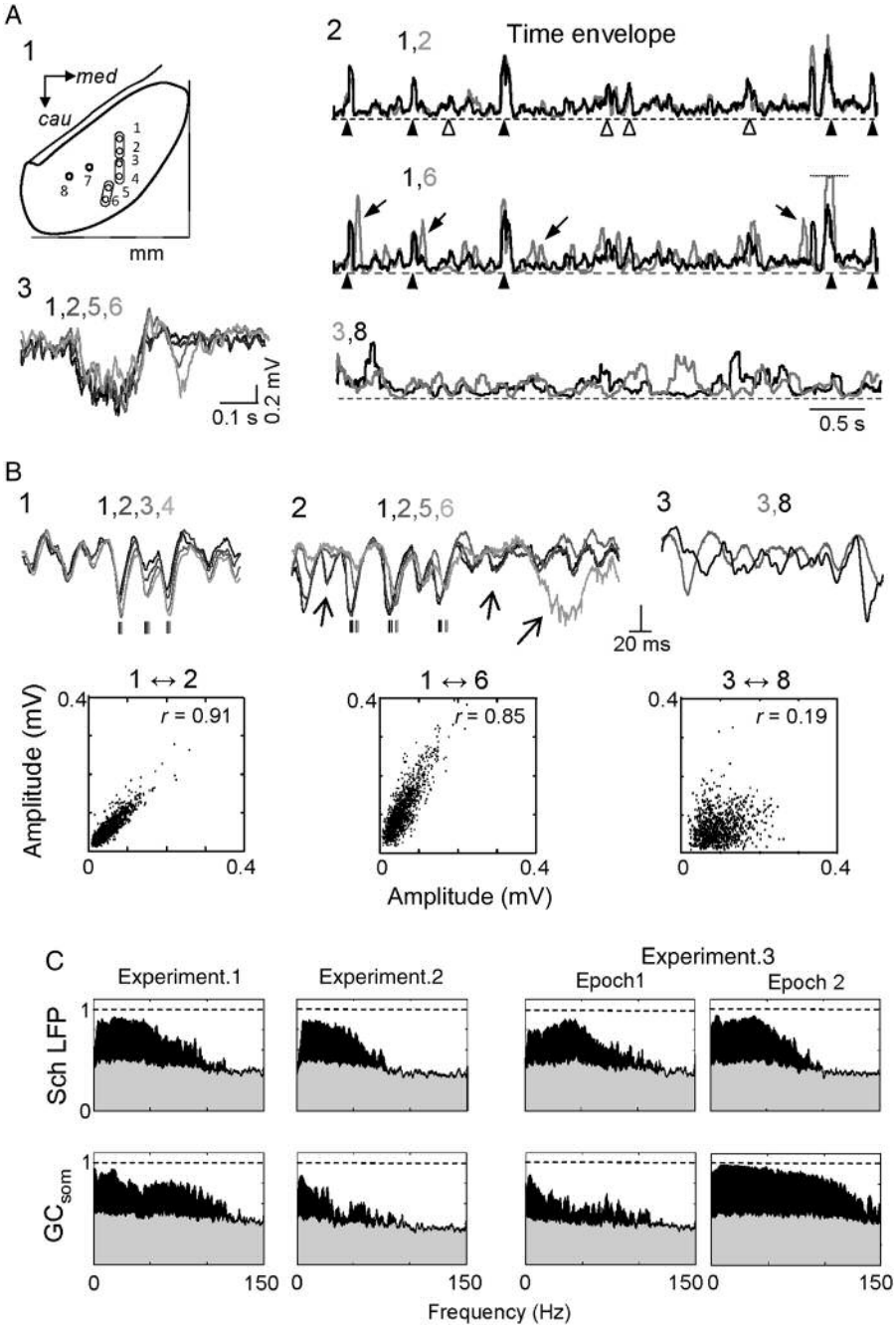

Figure 6. The fine temporal details within the modules of high spatial coherence indicate distinct mechanisms for the synchronous activation in different generators. (*A*) (1) Schematic showing the insertion points (dorsal view) of parallel linear arrays. (2) Time envelopes of instant power (sliding window of 0.1 s) for the Schaffer generator in different arrays, recording from loci parallel to the midline. Superimposed traces 1, 2 and 1, 6 belong to the same LFP epoch. The large bouts of activity correspond to SPWs. The spatial coverage of SPWs varied significantly, some reached the rostral end, while others did not (3). (*B*) Elementary μ-fEPSPs within the gamma frequency vary markedly within the series, but maintained proportional amplitude along large strips parallel to the midline, indicating a common origin and local substrate. The rostro-caudal delay matches spike conduction in Schaffer collaterals (vertical dashes indicate peak time and sequential activation). As recordings become more distant from one another (subplots 1–3), some of the quanta begin to exhibit amplitude differences (arrows), while the time course of SPWs differs normally. Comparisons between rostro-medial and ventro-lateral activations (3) are totally discrepant. The plots below show the amplitude covariation of paired quanta between arrays, where *r* is the cross-correlation coefficient for the paired data. These data indicate a heavy overlap of activated presynaptic axons as the substrate for the modules of high spatial coherence. (*C*) Comparative spectral coherence of 1 min epochs for the Schaffer (upper row) and GC_{som} (lower row) generators between pairs of electrode arrays separated by 0.5 mm in different experiments and epochs. Gray shading indicates the level of statistical significance (surrogate test). The Schaffer generator exhibits similar spectral profiles in all and for similar frequency ranges, while the GC_{som} inhibitory generator varied considerably even in different epochs of the same animal (t1 and t2 of Experiment 3). This discrepancy suggests the existence of different mechanisms underlying the high spatial coherence.

CA3, and medial entorhinal cortex, respectively. The average degree of ongoing synchronous firing in presynaptic units was enhanced by GABA blockade via local BIC administration through a recording pipette (Fig. 7*A*). Epileptic spikes developed locally at sites in the afferent population (open arrows in traces of Fig. 7*B*) that evoked fEPSPs in postsynaptic sites

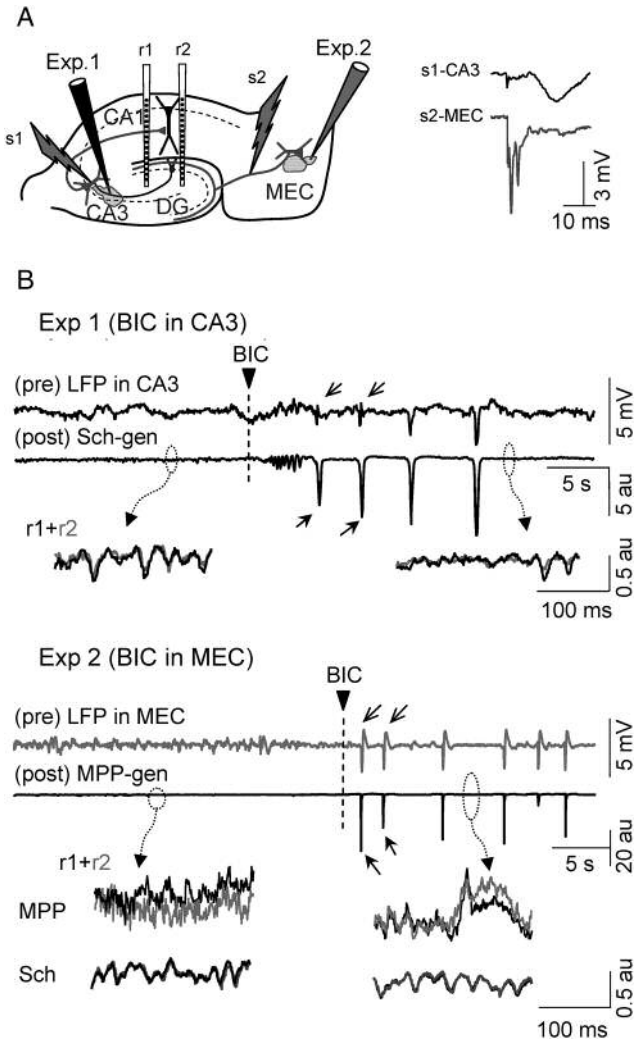

Figure 7. Spatial coherence of LFPs also depends on the synchrony of afferent populations. (*A*) The arrangement used for the experimental modulation of the spontaneous firing synchronism in presynaptic neurons that gives rise to hippocampal LFP generators. The Schaffer and MPP generators were obtained independently from LFP profiles in 2 parallel arrays (r1 and r2; 0.5 mm apart). Stimulating electrodes (S1 and S2) were placed in the ipsilateral CA3 and the medial portion of the angular bundle for the test activation of studied pathways. One injecting/recoding pipette filled with BIC was placed in either the CA3 somatic layer (Experiment 1) or the MEC. MEC-evoked responses to the right were recorded from the injecting pipette and guided placement. (*B*) The long traces correspond to raw LFPs recorded by injecting pipettes at afferent populations (pre), and to simultaneous time activation of the LFP generators in postsynaptic regions (post). Upon microdrop injection of a GABA blocker (BIC), epileptic spikes developed locally in both experiments (open arrows in CA3 and MEC traces of raw LFPs), which produced large synaptic envelopes in LFP generators (arrows in Sch and MPP traces). However, the correlation of baseline activity in periods between epileptic spikes only increased in the MPP generator. Although increased synchrony occurred in both afferent populations, it is only reflected in the LFP generator whose minimal module of spatial coherence is smaller than the recording interdistance (the MPP). Thus, while the temporal pattern of Schaffer activities may change, the correlation between loci activated by the same axons is unaffected, if it was already synchronous in control conditions.

(closed arrows), ensuring topological connection between the 2 regions. If our hypothesis is correct, there should be no variation in the correlation of LFP generators between pairs of postsynaptic sites that already had a strong correlation due to structural constraints, while increased afferent synchronization would be expected when there is low spatial coherence in control conditions. We examined postsynaptic sites 500 µm apart, and the instants of epileptic spikes were excluded. When BIC was injected into the CA3 (Fig. 7*B*, Experiment 1), local epileptic spikes developed in the raw LFP at the site of injection (pre-CA3 in Fig. 7*B*) that produced large fEPSPs in the postsynaptic CA1. Following ICA, these appeared selectively in the Schaffer LFP generator (post-CA1). The ongoing postsynaptic Schaffer gamma activity that was strongly correlated between pairs of sites in control conditions became distorted following the administration of BIC (enlarged traces below), although the intersite correlation remained high (0.88 ± 0.02 and 0.84 ± 0.01 in control and BIC conditions, respectively, $n = 6$ epochs). However, when BIC was injected into the medial entorhinal cortex (MEC; Fig. 7*B*, Experiment 2), the spatial correlation of the MPP generator obtained in pairs of postsynaptic DG sites increased notably (0.5 ± 0.02 and 0.77 ± 0.03 in control and BIC conditions, respectively).

Discussion

In general, it is difficult to interpret LFPs and their zonal divergence in situations where synaptic currents of different presynaptic origins combine. Using spatially discriminating techniques in the hippocampus, we have separated and analyzed up to 6 stable laminar LFP generators, each with distinct synaptic territories in specific domains of principal cells and hippocampal subfields, these matching known terminations of local and extrinsic presynaptic populations. LFP synaptic generators feature the minimum modules of spatial coherence that at least in one case (Schaffer) was modular-like and determined by the common topology of presynaptic units. Others are less regionalized and can be better explained by widespread coalescence of synaptic territories from presynaptic individual cell's axons, for example, the somatic inhibitory input to granule cells. We have shown that, for distant recordings separated more than the size of structural modules, the pathway-specific LFPs reflect the independent activity of distinct groups of units in the same presynaptic population, such that different modes of functional presynaptic firing can be recognized by the distinct spatial coverage of postsynaptic generators.

There is a general consensus that LFPs arise from synchronous currents in multicellular sources. While the theoretical bases of LFPs have been well described (Lorente de Nó 1947; Elul 1972; Klee and Rall 1977; Gloor 1985; Varona et al. 2000), there exists certain lag in their experimental application over involved neuronal structures. While data contingent with specific LFP events (e.g., unitary activity, intracellular recordings: Buzsáki et al. 1983) provides valuable hint on their cellular sources, the detailed information on the geometry and arrangement of unitary neuronal sources and activating inputs is required for a reliable and unambiguous identification. The ongoing activity involves the activation of individual cells or cell assemblies that may project to different parts of postsynaptic regions. Hence, the LFP activity generated by input from a single presynaptic population is not synchronous all over. Besides, different extrinsic and local populations have dissimilar axonal coverage of the dendritic domains in target cells, thus generating LFPs of different spatial distribution. The optimization of spatially discriminating techniques such as ICA enables the separation of LFPs in the hippocampus into individual generators with a constant spatial distribution

(Korovaichuk et al. 2010). By definition, pathway-specific generators exhibit full laminar coherence (as evoked potentials), which eliminates the inherent problems of varying polarity and amplitude when recording from different levels or strata. Accordingly, the time activation of the LFP generators can be used to establish their spatial extension by simple correlation of the activities recorded at different loci.

Most LFP Generators are Pathway Specific, but not all Synaptic Pathways Produce Observable LFPs

Like the evoked potential profiles generated by the specific activation of anatomical pathways (Andersen et al. 1971), ongoing LFP generators have smooth spatial distributions with a single maximum and a spatial distribution of inward/outward currents confined to the cellular axis of either the pyramidal or granule cells. Thus, the Schaffer, MPP, and LPP excitatory generators have active sinks in both the CA1 st. radiatum and the middle as well as outer thirds of the molecular layer, respectively. As expected, the activity of all these generators is selectively depressed by blocking glutamate receptors. In turn, the sink/source profiles for the GC_{som} and $CA3_{som}$ generators matched well with the expected profiles of somatic/perisomatic inhibitory synapses, and their activities were selectively abolished by GABA-R blockade. Therefore, these generators most likely correspond to basket-cell type inputs in each subfield. We obtained conflicting results for the strong LM generator, which was partially depressed by both Glu and GABA-A receptor blockades, and that displayed a temporal succession of sinks and sources. This dendritic domain may generate active sinks from perforant path activation (Leung and Peloquin, 2010) and active sources from Or-lac interneurons. One possible explanation is that the LM generator is a combination of 2 inputs that are difficult to separate by ICA, 1 excitatory and 1 inhibitory, which converge on the same dendritic domain at the distal tuft (Brankačk et al. 1993). The stability of all the LFP generators identified was confirmed by chronic recordings revealing the essentially identical subcellular and regional spatial distributions. Thus, we consider each LFP generator as a pathway-specific LFP component with populations of origin in the ipsilateral CA3, medial and lateral entorhinal cortices, and 3 different local inhibitory subnetworks: 2 of the basket type in CA3 and GC, and a distal-projecting subnetwork in the CA1 field.

It is noteworthy that the anatomical connections whose synchronous activation produce measurable evoked field potentials outnumber the hippocampal LFP generators described here. Among the unrepresented inputs are those from the septum, the contralateral (commissural) inputs to the CA1 and CA3, and a number of local inhibitory inputs in all subfields (Andersen et al. 1961; Amaral 1978; Buzsaki and Eidelberg 1982; Somogyi and Klausberger 2005). However, not all synaptic currents contribute significantly to macroscopic LFPs, rather only those that conform to the appropriate spatial structure and temporal pattern (Elul 1972; Makarova et al. 2011; Ho et al. 2012). Thus, poor laminar segregation of axonal arborization, or extreme levels of activity (too scarce or too frequent), would not generate a sufficient extracellular current or the required time fluctuation, but they are still essential for information processing and postsynaptic output.

Functional Implications of Pathway-Specific Structural Boundaries of LFP Coherence

The CA1 Schaffer and the MPP entorhinal inputs exhibit significantly different modules of spatial coherence in spite of the similar temporal structure of their respective ongoing activities with dominant excitatory quanta in gamma frequencies (Fernández-Ruiz, Makarov, Benito, et al. 2012; Fernández-Ruiz, Makarov, Herreras 2012). For these inputs, presynaptic neurons project axons that branch out and leave multiple buttons en passage, which should produce near-synchronous LFPs over an extended postsynaptic area. Therefore, the differential minimal spatial modules are probably due to additional anatomical factors, such as the degree of the spatial overlap of axonal territories of individual cells. Schaffer LFPs are highly coherent within 2×0.5 mm sheets that lie roughly parallel to the midline in the dorsal hippocampus, which is approximately the extension of a single CA3 pyramidal cell axonal arborization in the CA1 (Ishizuka et al. 1990), although they fall off sharply in the lateral direction beyond 0.5 mm. The covariance of the amplitude and the characteristic rostro-caudal delay of elementary μ-fEPSPs can only be explained by near-synchronous activation of multiple CA1 pyramidal cells by axons with dominant rostro-caudal orientation and a similar topology originating in groups of simultaneously firing CA3 pyramidal cells (Hjorth-Simonsen 1973; Li et al. 1994; Fig. 8*A*). For recording positions separated laterally by larger distances, the increasing divergence of Schaffer LFPs reflects the independent activity of distinct subsets of presynaptic CA3 neurons. Thus, the basal activity of the Schaffer generator is reminiscent of the lamellar concept proposed by Andersen et al. (1971), at least for this segment of the hippocampal network. However, the longitudinal CA3–CA1 communication that is also present (Li et al. 1994) may not be based on functional assemblies with overlapping topological projections. The Schaffer SPWs represent a notable nonlamellar exception that cover much larger and more variable zones of the CA1, which is slowly activated in spatial sequence without an apparent preferred direction, and that can stop suddenly at different sites. These features are compatible with a slow avalanche-like longitudinal activation of CA3 units over extended septo-temporal levels, possibly through the local recurrent network (e.g., Vincent et al. 2012). Thus, the differential spatial coverage of SPWs and μ-fEPSPs reflect 2 modes and degrees of synchronization in presynaptic CA3 units.

In turn, the extremely low spatial correlation of LFPs produced by the MPP is indicative of highly localized clusters of postsynaptic activity. Such a pattern may result from the spatial divergence of individual perforant pathway axons, while the strong curvature of the DG could further minimize extracellular clustering of synaptic currents, even for synchronous events (Fig. 8*B*). This implies that the use of different recording sites permits a more topological reading of the ongoing activity of presynaptic entorhinal cells. The obvious impractical consequence is that one-site recordings of the activity of the MPP generator cannot be taken as a representative of entorhinal population activity.

We have demonstrated that inhibitory inputs can act as strong LFP generators. Notably the inhibitory plexuses of individual interneurons extend over distances shorter than the size of coherent modules (Somogyi and Klausberger 2005). To reconcile these findings, we may suppose that multiple

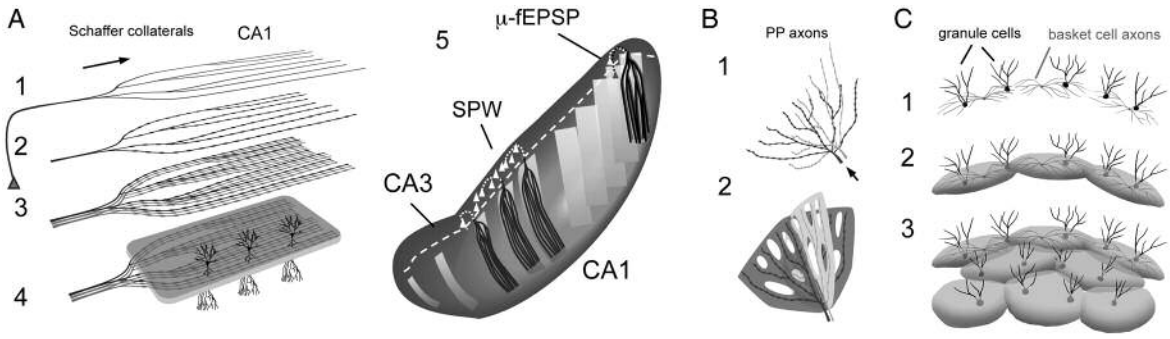

Figure 8. Proposed structural and functional determinants of spatial coherence for some hippocampal LFP generators. (*A*) Excitatory Schaffer input to CA1. Each CA3 pyramidal neuron sends axon that leaves multiple collaterals in CA1 with dominant parallel orientation (1) leaving synaptic buttons en passant (2) on numerous CA1 pyramidal cells. Functional CA3 pyramidal cell assemblies have similar axonal territories (3) and their joint activation produces near-synchronous synaptic currents on a narrow dendritic band of CA1 pyramidal cells (4) that conforms a strip-like spatial module of coherent LFP activity. The width of the strip is thus defined by the average coverage of individual cell's axon and the common topology of a functional CA3 assembly. Note that the same spatial module can be "occupied" by different CA3 assemblies as long as they have similar topology (e.g., sequence of μ-fEPSPs). The apparent "lamellar" organization (5) manifests at different septo-temporal levels of the CA1, but is broken up when afferent firing synchrony organizes differently, as during SPWs in which cofiring CA3 neurons extend over widespread septo-temporal levels. (*B*) Perforant path input. The LFP activity is poorly correlated in nearby sites, possibly because of the fanning of axon branches (1) and reduced spatial overlap of synchronous synaptic currents caused by excessive curvature. (*C*) Granule cell somatic inhibition (GC_{som} generator). The axonal plexus of basket-cell interneurons (in gray) may produce inhibitory currents in the somata of the large number of granule cells (in black). (2, 3) Synchronous modulation of basket-cell subpopulation produces the coalescence of basket-cell synaptic territories, thus spatial coherence of the GC_{som} generator extends much more than the extension of one cell's axonal plexus.

homogeneous interneurons forming functional subnetworks are jointly modulated by an external driver or are mutually synchronized. Accordingly, the inhibitory currents produced by axons from individual interneurons merge in large steady modules (Fig. 8*C*). This concept coincides with functional results that propose correlated activity in interneuron subnetworks (Whittington et al. 1995; Fukuda and Kosaka, 2000; Ho et al. 2012). Interestingly, we observed variations in the spectral coherence between 2 readings of the GC_{som} inhibitory generator despite a steady strong global correlation. We propose that this may be a manifestation of functional coupling/decoupling mechanisms of the units in the subnetwork according to the information-processing demands.

We presented evidence demonstrating that the more presynaptic neurons fire synchronously (as witnessed by the occurrence of local epileptic spikes following disinhibition), the greater the spatial correlation of LFPs in the postsynaptic region, presumably by blending together coactivated postsynaptic territories. As expected, this only occurs for the medial entorhinal cortex projections in the DG that normally exhibit low spatial correlation, but not for the Schaffer input to CA1 that has full coherence, at least within longitudinal strips. This result provides empirical evidence supporting the notion that both spatial (overlap of axonal territories) and temporal factors (their synchronous activation) play an important role in the generation of LFPs. Moreover, our findings highlight the peculiar transformation of synchronization in presynaptic units into postsynaptic coherence, that is, temporal into spatial features of activity, which is essential to interpret zonal LFP differences. Thus, firing synchronization of all afferent fibers in a pathway, as by electric shocks, produces the complete and nearly synchronous activation of the entire postsynaptic region, that is, full spatial coherence of the recorded field potential activity. However, during ongoing activity, only groups of afferent neurons fire correlated spikes, and their axons activate varying portions of the postsynaptic region according to the topology of connections; hence, spatial coherence of LFPs decreases. Since LFPs are the reflection of spiking activity in presynaptic populations, the found stereotyped spatial patterns of LFP coherence, as seen in Schaffer μ-fEPSPs, or inhibitory GC_{som} potentials, denote the specific temporal patterns of the activation of presynaptic units.

The physiological relevance of spatial coherence is that it helps us discerning when 2 recording sites are capturing the same information from afferent neuron populations. Matching LFPs is either due to overlapping axonal territories of presynaptic units (whether firing synchronously or not) or to the synchronous firing of presynaptic cells (whether their axons overlap in target regions). However, differing LFPs necessarily indicates varying activity in presynaptic units. Naturally, this is only applicable to pathway-specific LFPs. In conclusion, the finding of pathway-specific modules of LFP activity serves not only to reveal the topology of connections, but also explains LFP differences in nearby recordings. This represents a necessary first step to mapping their temporal changes in activity and their correlations with full understanding of their biophysical bases.

Supplementary Material

Supplementary material can be found at: http://www.cercor.oxfordjournals.org/.

Funding

This work was supported by the former Spanish Ministry of Science and Innovation (BFU2010-19192/BFI and FIS2010-20054).

Notes

We thank S. Montgomery and G. Buzsáki for providing LFP recordings in awake animals, C. Dotti and G. Martín-Vázquez for helpful comments, R. Núñez and J. Delgado for technical assistance and help with graph art, and M. Sefton at BiomedRed for editorial support.

References

Amaral DG. 1978. A Golgi study of cell types in the hilar region of the hippocampus in the rat. J Comp Neurol. 182:851–914.

Andersen P, Bliss TVP, Skrede KK. 1971. Lamellar organization of hippocampal excitatory pathways. Exp Brain Res. 13:222–238.

Andersen P, Bruland H, Kaada BR. 1961. Activation of the field CA-1 of the hippocampus by septal stimulation. Acta Physiol Scand. 51:29–40.

Arieli A, Shoham D, Hildesheim R, Grinvald A. 1995. Coherent spatiotemporal patterns of ongoing activity revealed by real-time optical imaging coupled with single-unit recording in the cat visual cortex. J Neurophysiol. 73:2072–2093.

Bach M, Krüger J. 1986. Correlated neuronal variability in monkey visual cortex revealed by a multi-microelectrode. Exp Brain Res. 61:451–456.

Belitski A, Gretton A, Magri C, Murayama Y, Montemurro MA, Logothetis NK, Panzeri S. 2008. Low-frequency local field potentials and spikes in primary visual cortex convey independent visual information. J Neurosci. 28:5696–5709.

Bell A, Sejnowski T. 1995. An information-maximization approach to blind separation and blind deconvolution. Neural Comput. 7:1129–1159.

Brankačk J, Stewart M, Fox SE. 1993. Current source density analysis of the hippocampal theta rhythm: associated sustained potentials and candidate synaptic generators. Brain Res. 615:310–327.

Buzsáki G, Eidelberg E. 1982. Convergence of associational and commissural pathways on CA1 pyramidal cells of the rat hippocampus. Brain Res. 237:283–295.

Buzsáki G, Leung LS, Vanderwolf CH. 1983. Cellular bases of hippocampal EEG in the behaving rat. Brain Res. 287:139–171.

Canals S, López-Aguado L, Herreras O. 2005. Synaptically-recruited apical currents are required to initiate axonal and apical spikes in hippocampal pyramidal cells: modulation by inhibition. J Neurophysiol. 93:909–918.

Canning KJ, Leung LS. 1997. Lateral entorhinal, perirhinal, and amygdale-entorhinal transition projections to hippocampal CA1 and dentate gyrus in the rat: a current source density study. Hippocampus. 7:643–655.

Chen A. 2006. Fast kernel density independent component analysis. Lecture Notes Comput Sci. 3889:24–31.

Choi S, Cichocki A, Park HM, Lee SY. 2005. Blind source separation and independent component analysis: a review. Neur Inf Process Let Rev. 6:1–57.

Congedo M, John RE, De Ridder D, Prichep L. 2010. Group independent component analysis of resting state EEG in large normative samples. Int J Psychophysiol. 78:89–99.

Diesmann M, Gewaltig MO, Aertsen A. 1999. Stable propagation of synchronous spiking in cortical neural networks. Nature. 402:529–533.

Elul R. 1972. The genesis of the EEG. Int Rev Neurobiol. 15:228–272.

Fernández-Ruiz A, Makarov VA, Benito N, Herreras O. 2012. Schaffer-specific local field potentials reflect discrete excitatory events at gamma-frequency that may fire postsynaptic hippocampal CA1 units. J Neurosci. 32:5165–5176.

Fernández-Ruiz A, Makarov VA, Herreras O. 2012. Sustained increase of spontaneous input and spike transfer in the CA3-CA1 pathway following long term potentiation in vivo. Front Neural Circuits. 6:71.

Freeman JA, Nicholson C. 1975. Experimental optimization of current source-density technique for anuran cerebellum. J Neurophysiol. 38:369–382.

Fukuda T, Kosaka T. 2000. Gap junctions linking the dendritic network of GABAergic interneurons in the hippocampus. J Neurosci. 20:1519–1528.

Gloor P. 1985. Neuronal generators and the problem of localization in electroencephalography: application of volume conductor theory to electroencephalography. J Clin Neurophysiol. 2:327–354.

Golarai G, Sutula TP. 1996. Bilateral organization of parallel and serial pathways in the dentate gyrus demonstrated by current-source density analysis in the rat. J Neurophysiol. 75:329–342.

Herreras O. 1990. Propagating dendritic action potential mediates synaptic transmission in CA1 pyramidal cells in situ. J Neurophysiol. 64:1429–1441.

Herreras O, Solís JM, Muñoz MD, Martín del Río R, Lerma J. 1988. Sensory modulation of hippocampal transmission. I. Opposite effects on CA1 and dentate gyrus synapsis. Brain Res. 451:290–302.

Hjorth-Simonsen A. 1973. Some intrinsic connections of the hippocampus in the rat: an experimental analysis. J Comp Neurol. 147:145–162.

Ho ECY, Strüber M, Bartos M, Zhang L, Skinner FK. 2012. Inhibitory networks of fast-spiking interneurons generate slow population activities due to excitatory fluctuations and network multistability. J Neurosci. 32:9931–9946.

Hutchison RM, Mirsattari SM, Jones CK, Gati JS, Leung LS. 2010. Functional networks in the anesthetized rat brain revealed by independent component analysis of resting-state fMRI. J Neurophysiol. 103:3398–3406.

Ishizuka N, Weber J, Amaral DG. 1990. Organization of intrahippocampal projections originating from CA3 pyramidal cells in the rat. J Comp Neurol. 295:580–623.

Klee M, Rall W. 1977. Computed potentials of cortically arranged populations of neurons. J Neurophysiol. 40:647–666.

Korovaichuk A, Makarova J, Makarov VA, Benito N, Herreras O. 2010. Minor contribution of principal excitatory pathways to hippocampal LFPs in the anesthetized rat: a combined independent component and current source density study. J Neurophysiol. 104:484–497.

Leung LS. 1979. Potentials evoked by alvear tract in hippocampal CA 1 region in rats. II. Spatial field analysis. J Neurophysiol. 42:1571–1589.

Leung LS, Péloquin P. 2010. Cholinergic modulation differs between basal and apical dendritic excitation of hippocampal CA1 pyramidal cells. Cereb Cortex. 20:1865–1877.

Li XG, Somogyi P, Ylinen A, Buzsáki G. 1994. The hippocampal CA3 network: an in vivo intracellular labeling study. J Comp Neurol. 339:181–208.

López-Aguado L, Ibarz JM, Herreras O. 2001. Activity-dependent changes of tissue resistivity in the CA1 region in vivo are layer-specific: modulation of evoked potentials. Neuroscience. 108:249–262.

Lorente de Nó R. 1947. Analysis of the distribution of action currents of nerves in volume conductors. In: A study of nerve physiology. part 2, vol. 132. New York: The Rockefeller Institute, p. 384–477.

Lorente de Nó R. 1934. Studies on the structure of the cerebral cortex. II. Continuation of the study of the ammonic system. J Psychol Neurol. 46:113–177.

Makarov VA, Makarova J, Herreras O. 2010. Disentanglement of local field potential sources by independent component analysis. J Comp Neurosci. 29:445–457.

Makarova J, Ibarz JM, Makarov VA, Benito N, Herreras O. 2011. Parallel readout of pathway-specific inputs to laminated brain structures. Front Syst Neurosci. 5:77.

Makeig S, Jung TP, Bell AJ, Ghahremani D, Sejnowski TJ. 1997. Blind separation of auditory event-related brain responses into independent components. Proc Natl Acad Sci USA. 94:10979–10984.

McNaughton BL. 1980. Evidence for two physiologically distinct perforant pathways to the fascia dentata. Brain Res. 199:1–19.

Montgomery SM, Betancur MI, Buzsáki G. 2009. Behavior-dependent coordination of multiple theta dipoles in the hippocampus. J Neurosci. 29:1381–1394.

Nunez PL, Srinivasan R. 2006. Electric fields of the brain: the neurophysics of EEG. 2nd ed. New York: Oxford University Press.

Paulsen O, Moser EI. 1998. A model of hippocampal memory encoding and retrieval: GABAergic control of synaptic plasticity. Trends Neurosci. 21:273–278.

Plonsey R. 1969. Bioelectric phenomena. New York: McGraw-Hill.

Purpura DP. 1959. Nature of electrocortical potentials and synaptic organizations in cerebral and cerebellar cortex. Int Rev Neurobiol. 1:47–163.

Rappelsberger P, Pockeberger H, Petsche H. 1981. Current source density analysis: methods and application to simultaneously recorded field potentials of the rabbit's visual cortex. Pfluegers Arch. 389:159–170.
Reichinnek S, Künsting T, Draguhn A, Both M. 2010. Field potential signature of distinct multicellular activity patterns in the mouse hippocampus. J Neurosci. 30:15441–15449.
Schreiber T, Schmitz A. 2000. Surrogate time series. Physica D. 142:646–652.
Somogyi P, Klausberger T. 2005. Defined types of cortical interneurone structure space and spike timing in the hippocampus. J Physiol. 562:9–26.
Traub RD, Spruston N, Soltesz I, Konnerth A, Whittington MA, Jefferys GR. 1998. Gamma-frequency oscillations: a neuronal population phenomenon, regulated by synaptic and intrinsic cellular processes, and inducing synaptic plasticity. Prog Neurobiol. 55:563–575.
van de Ven VG, Formisano E, Prvulovic D, Roeder CH, Linden DEJ. 2004. Functional connectivity as revealed by spatial independent component analysis of fMRI measurements during rest. Hum Brain Mapp. 22:165–178.
Varona P, Ibarz JM, López-Aguado L, Herreras O. 2000. Macroscopic and subcellular factors shaping CA1 population spikes. J Neurophysiol. 83:2192–2208.
Vincent K, Tauskela JS, Thivierge JP. 2012. Extracting functionally feedforward networks from a population of spiking neurons. Front Comput Neurosci. 6:86.
Whittington MA, Traub RD, Jefferys JGR. 1995. Synchronized oscillations in interneuron networks driven by metabotropic glutamate receptor activation. Nature. 373:612–615.
Woodbury JW. 1960. Potentials in a volume conductor. In: Ruch TC, Fulton JF, editors. Medical physiology and biophysics. Philadelphia and London: WB Saunders Co. p. 83–91.